Observation of ponderomotively driven bow shock using Thomson scattering

A L Milder, C Bruulsema, S Hüller, C Walsh, W Rozmus, L Yin, J Ludwig, W A Farmer, B J Albright, H A Rose, et al.

Observation of ponderomotively driven bow shock using Thomson scattering

A. L. Milder,[1,2,*] C. Bruulsema,[3] S. Hüller,[4] C. Walsh,[3] W. Rozmus,[2] L. Yin,[5]
J. Ludwig,[3] W. A. Farmer,[3] B. J. Albright,[5] H. A. Rose,[5] and G. Swadling[3]

[1]*Laboratory for Laser Energetics, 250 E. River Rd, Rochester, NY 14623, USA*
[2]*Department of Physics, University of Alberta, Edmonton, Alberta T6G 2E1, Canada*
[3]*Lawrence Livermore National Laboratory, 7000 East Avenue, Livermore, CA 94550, USA*
[4]*Centre de Physique Théorique (CPHT), CNRS,*
Ecole Polytechnique, IP Paris, Palaiseau, France
[5]*Los Alamos National Laboratory, P.O Box 1663, Los Alamos, NM 87545, USA*

(Dated: January 29, 2025)

High energy speckled lasers are known to exert ponderomotive forces on a plasma, this can reduce flow transverse to the propagation of the beams. When coupled with a supersonic flow, this has been shown to lead to formation of a shock that travels against the flow. Experiments conducted on the OMEGA laser facility have used Thomson scattering to observe density and velocity changes consistent with this ponderomotively driven shock. Comparisons of the data with hydrodynamic simulations with the ponderomotive force, particle-in-cell simulations with a full Maxwell field solver, and hydrodynamic simulations without the ponderomotive force show that this shock feature is only reproduced with accounting for the ponderomotive force.

Understanding laser propagation in inhomogeneous plasmas remains a challenge for many plasma physics experiments, especially those with complex geometries such as inertial confinement fusion (ICF). Over the past 10 years, significant effort has been made to understand and improve the coupling and accounting of laser drive in inertial confinement fusion (ICF) experiments [1–3]. Simulations of hydrodynamically complex experiments often treat laser propagation with ray-based models that consider refraction, absorption, and instability thresholds but do not attempt to self-consistently solve Maxwell's equations due to the scale separation and computational expense. This results in ignoring effects such as the ponderomotive force and plasma response, effects that can significantly affect the laser propagation.

Previous theoretical studies have shown that intense lasers are deflected in a flowing plasma due to the nonlinear plasma response even for intensities well below the threshold for ponderomotive self-focusing[4, 5]. The ponderomotive force causes electrons to be pushed from higher- to lower-intensity regions of the laser spot digging a well in the density profile. In the case of a flowing plasma, these density wells are pushed downstream, resulting in tilted density perturbations that are no longer symmetric about the high-intensity spots [6]. The laser refracts over the local density gradient and, due to conservation of momentum, this applies a drag force on the flowing plasma. This process has the potential to impact beam pointing [7] and the seed from which laser-plasma instabilities such as stimulated Brillouin scattering can grow.

When the drag caused by the ponderomotive force slows the plasma flow from super-sonic to sub-sonic, a shock is generated that propagates against the direction of flow or upstream. In the case of speckled beams often used in ICF, each speckle independently perturbs the density and flow. These perturbations coalesce into a shock as they break out of the beam, the single shock front then travels upstream [8, 9].

This article demonstrates the first observation of a ponderomotively driven shock, using Thomson scattering to observe the resultant plasma conditions upstream and downstream of the shock generation region. Measured plasma conditions showed the expected features of this shock, a density spike was observed upstream of the beams used to provide the ponderomotive slowing, and was co-timed with a transition from super-sonic to subsonic flow. Downstream a reduction of the density was observed, consistent with the ponderomotive force inhibiting the plasma flow. Two hydrodynamic simulation codes and one particle-in-cell code were utilized to elucidate the underlying physics. Simulations excluding the ponderomotive force failed to demonstrate the features ascribed to the shock. In contrast, simulations incorporating the ponderomotive force qualitatively replicated all the main observables.

Experiments designed to observe the ponderomotively driven bow shock were conducted on the OMEGA Laser System [10] at the Laboratory for Laser Energetics. Figure 1 shows the experimental configuration in which four ultraviolet (351 nm UV) laser beams were used to ablate an aluminum disk 25 µm thick with a diameter of 1.0 mm, producing a plasma plume that expanded away from the target. Four UV drive beams were focused 100 µm past the front surface of the target and used 300 µm diameter distributed phase plates to provide uniform illumination. The drive beams had a 3.7-ns pulse duration, full-width at half-maximum (FWHM), and 217 J per beam providing an on target intensity of $I_{\mathrm{UV}}^{\mathrm{drive}} = 2.5 \times 10^{14}$ W/cm^2.

To drive the shock 18 heater beams were focused at f/6.7, 600 µm away from the front, driven side, of the target (Fig 1 location B). These heater beams used

* Corresponding Author: amild@lle.rochester.edu

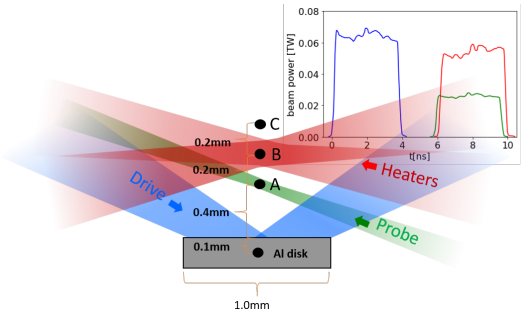

FIG. 1. Schematic of the experimental configuration. Four UV beams (blue) are used to ablate the aluminum target producing a plume which flows toward the heating beams (red). The heating beams (red) are focused at location B 600 µm above the target to ponderomotively drive a shock. A probe beam (green) can be pointed to location A or C in order measure plasma conditions with Thomson scattering upstream or downstream of the heater beams.

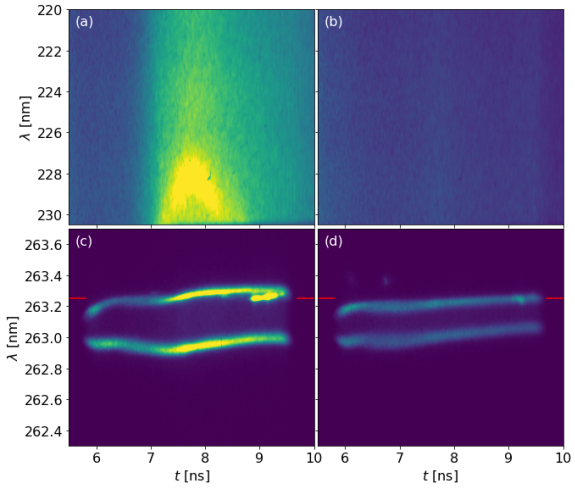

FIG. 2. Temporally resolved electron plasma wave (a,b) Thomson-scattering data and ion-acoustic wave (c,d) Thomson-scattering data upstream of the heating beam location. A red line indicates the probe wavelength on the ion-acoustic spectra (c,d). (a,c) were taken with the heating beams on while (b,c) have the heating beams turned off.

the same pulse shape and distributed phase plates as the drive beams producing an overlapped intensity of $I_{\mathrm{UV}}^{\mathrm{heater}} = 1.4 \times 10^{15}$ W/cm^2. The heater beams were delayed 6 ns from the start of the drive beams, 2.3 ns from the end of the drive beams (Fig. 1 inset), giving the expanding plasma time to cool and slow down, reaching ideal conditions to generate a shock. This delay was specifically tuned to provide a flow, perpendicular to the laser-propagation direction, near Mach 1 in the crossing beam region after the heating caused by the crossing beams. None of the beams used in this experiment used polarization smoothing or smoothing by spectral dispersion.

A 90-J UV (263.3 nm) probe beam was used to perform Thomson-scattering measurements of the plasma conditions upstream and downstream of the heater beams, during the shock generation. The probe beam used the same 3.7 ns pulse shape (Fig. 1 inset) delayed 5.8 ns from the start of the drive beams, 2.1 ns from the end of the drive beams, and a distributed phase plate to produce a smaller spot, 100-µm FWHM diameter, with an intensity of $I_{4\omega} = 3.1 \times 10^{14}$ W/cm^2. To measure the plasma conditions upstream of the heating beams, the probe was focused 400 µm from the front of the target (Fig 1 location A) and 800 µm from the front of the target to measure the conditions downstream (Fig 1 location C).

Thomson scattering data taken upstream of the heating beams (Fig. 2) show a transient density spike consistent with a shock traversing the Thomson volume. This density spike can be seen by the presence of an electron plasma wave feature in Fig. 2(a). The shift of this feature from the probe wavelength of 263.3 nm is correlated with the density, showing the density rises rapidly from 7 ns to roughly 7.8 ns when it begins to fall again. The strength of the signal in the ion-acoustic wave (IAW) spectra is also correlated to the electron density and a corresponding increase in signal was seen starting at 7.5 ns (Fig. 2c). Figure 2(b,d) show the same spectra without the heating beams. In this case, no increase in signal strength was observed in the ion-acoustic wave data, and the electron density remained too low for the electron plasma wave to be observed. The lack of an increased density without the crossing beams shows that the increased density originates with the heating beams, not the target or probe beam, and is therefore traveling upstream.

Figure 2(c) shows this density spike is also correlated with the flow approaching Mach 1. The separation of the ion acoustic wave features is proportional to twice the ion sound speed, and both peaks are Doppler-shifted due to the plasma flow. Consequently, when the flow is $\approx c_s$ the red-shifted peak crosses the probe's vacuum wavelength as observed at roughly 7.5 ns. The ion sound speed $c_s \approx 190 km/s$ is calculated from the measured electron temperature and an assumed ionization state of 11, the ion temperature correction is ignored as $T_e/T_i \gtrsim 4$.

Figure 3 shows the measured electron densities and flow velocities quantitatively compared to the results of hydrodynamic simulations using the code GORGON [11]. Measured plasma conditions were found by matching the collisionless spectral density function [12] to the measured Thomson spectra (Fig. 2). The extended-MHD code GORGON [13, 14] was used to simulate the hydrodynamic evolution of the plasma without the effects of ponderomotive forces. These simulations were conducted in a 2D cylindrical geometry (r, z) with the longitudinal axis (z) along the target normal. Laser propagation and heating was resolved in 3D using ray-tracing and inverse bremsstrahlung absorption. GORGON has previously been used to model laser interactions with planar targets, giving reasonable agreement to proton radiography measurements of self-generated electromag-

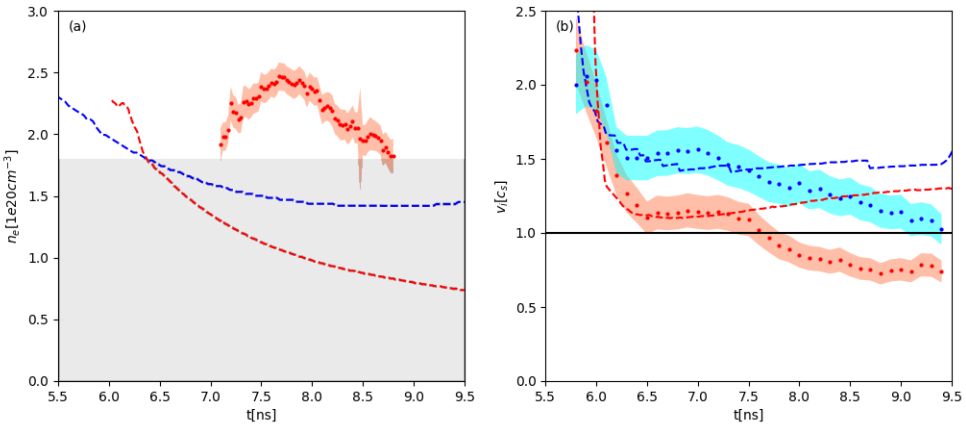

FIG. 3. Plasma conditions upstream of the heater beams measured with Thomson scattering and predicted by simulations. (a) electron density as a function of time from experimental data with heater beams (red circles). A gray shaded region denotes the range not visible in the Thomson scattering data. (b) flow velocity in units of ion sound speed as a function of time from experimental data with heater beams (red circles) and without heater beams (blue circles). Density (a) and velocity (b) predictions from hydro-dynamic simulations are given with (red dashed curves) and without (blue dashed curves) heating beams.

netic fields [15, 16]. Since the simulation with GORGON did not include the ponderomotive force it helps identify whether changes in the plasma conditions were caused by the additional heating of the 18 heating beams or the ponderomotive shock.

Figure 3(a) shows the electron density upstream of the heating region. The transient density spike was observed, as in fig. 2(a), peaking at 7.8 ns and a density of 2.5×10^{20} cm^{-3}. These simulations put the density with no crossing beams below the detection threshold ($\approx 1.8\times10^{20}cm^{-3}$) for this spectrometer configuration, which is consistent with the lack of an observed electron plasma wave feature in this case (Fig. 2b). The density simulated with crossing beams is even lower due to increased heating. The upstream measured density with the crossing beams on significantly exceeds that of the no-shock model provided by the simulations and has a qualitatively different shape only decreasing in time, indicating that the observed increase is caused by the ponderomotive coupling, which is absent in GORGON simulations.

Flow velocity measurements upstream of the heating region in figure 3(b) present the same story. In both simulations and measurements, the flow in the crossing beam case approaches Mach 1 around 6.5 ns and is sustained for a nanosecond. These are the ideal conditions for shock formation, an incoming flow near Mach 1, sustained so that the shock has time to develop. For experimental points (circles), the sound speed was determined from the data, and for simulations the sound speed was extracted from the simulation. Both the flow and density observations are consistent with a shock front consisting of a density spike and super-sonic/sub-sonic transition passing through the observation point. The resulting perturbation is therefore traveling super-sonically relative to the plasma, identifying it as a true shock.

Plasma conditions downstream without heating beams show excellent quantitative agreement with GORGON simulations (Fig. 4), demonstrating their capability to predict the plasma conditions in the absence of the ponderomotive force and its effects. For the downstream data, the EPW spectrometer was adjusted to measure a spectral range that corresponds to lower densities. Density and flow were found to decrease in time as the plume expands into vacuum. A small increase in temperature is seen around 6.0 ns due to heating from the Thomson probe beam.

With the heater beams on, the measured downstream plasma conditions (Fig. 4) were consistent with the plasma flow being restrained by the ponderomotive force. As the plasma is slowed due to ponderomotive drag, and a shock is launched upstream, the decreased flow velocity into heated region causes the density to fall. This can be seen in (Fig. 4a). This region of plasma also experienced significant heating due to the crossing beams present, decreasing the normalized flow. The GORGON simulations show this decrease in density was more then expected due to the heating alone.

At 8 ns the density, temperature, and velocity rapidly rose. As the simulated parameters do not shift at this time, the change appears to be caused by the ponderomotive effects and the associated shock. It is hypothesized that at 8 ns the incoming flow is no longer super-sonic and the ponderomotive force is no longer effective at holding the plasma back. This would result in hot plasma from the crossing beam region flowing downstream. Further experimental and simulation work is required to prove this hypothesis.

Fluid simulations of the isothermal plasma using a ver-

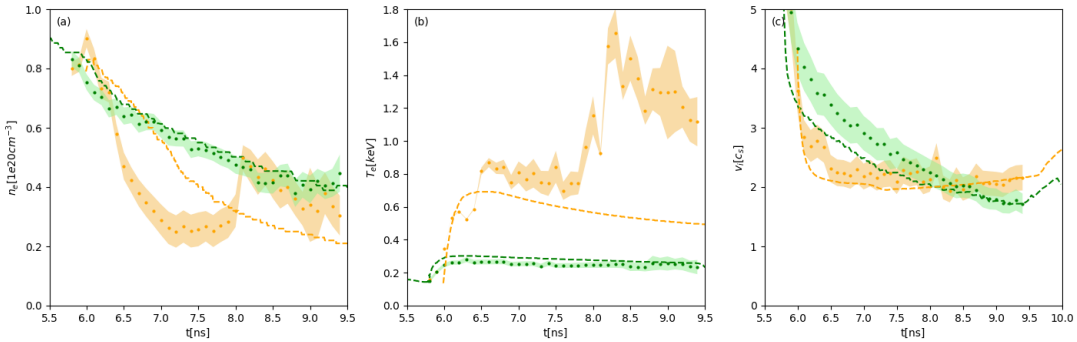

FIG. 4. Plasma conditions downstream of the heater beams measured with Thomson scattering and predicted by simulations. (a) electron density as a function of time from experimental data with (orange circles) and without (green circles) heater beams. (b) electron temperature as a function of time from experimental data with (orange circles) and without (green circles) heater beams. (c) flow velocity in units of ion sound speed as a function of time from experimental data with (orange circles) and without (green circles) heater beams. Corresponding predictions from hydro-dynamic simulations are given for each parameter with (orange dashed curves) and without (green dashed curves) heating beams.

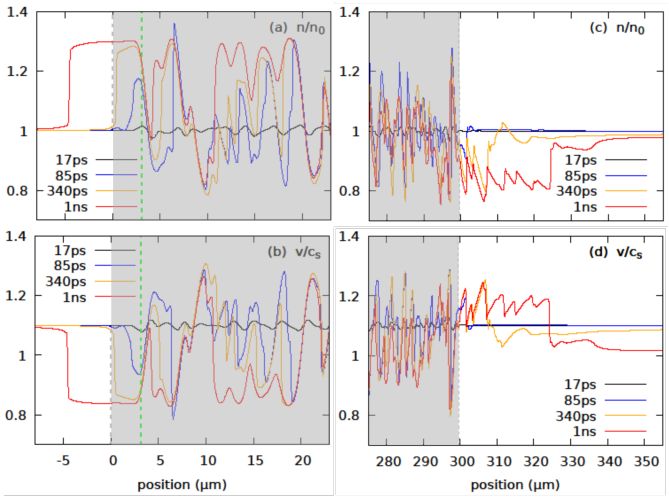

FIG. 5. Fluid simulations including the ponderomotive force. (a),(c) electron density normalized to the background density of 2.5 × 10^{20} cm^{-3} and (b),(d) flow velocity normalized to the sound speed as a function of position with respect to the left beam boundary (y =0) along the flow direction. Four temporal slices, zoomed over the front part in (a) and (b) and the rear part in (c) and (d), are shown at 17ps (black curve), 85ps (blue), 340ps (orange), and 1 ns (red) where $t = 0$ corresponds to 7.0 ns in the experiment. The shaded regions are within the beam spot, the green dashed lines in (a,b) the position of the first transition to subsonic flow y_{sonic}.

sion of the CLAWPACK [17] code, solve the nonlinear continuity and momentum equations, including the ponderomotive force due to the speckled laser beam [8]. The 2D geometry of these simulations describes the plasma response, including shock generation in the plane of the plasma flow across the laser beam. For the experimental parameters listed above, simulations (Fig. 5) were able to qualitatively capture most of the features observed in the experiment (Figs. 3, 4). Figure 5(a) shows a density spike associated with a shock propagating upstream, as observed in Figure 3(a), and a density deficit forming downstream of the crossing beams, as observed in Figure 4(a). Similarly, the simulated fluid velocities in Figure 5(b) show the supersonic/subsonic interface traveling upstream, as observed in Figure 3(b). These features are smaller in magnitude than those observed in the experiment due to the limited physics included in the code.

The conditions to generate the shock ponderomotively can be found by comparing the laser spot size and duration to the penetration depth required to reduce the flow to a sub-sonic speed and the time required for shock breakout. Using Eq. 22 from Ref. [8] an incoming flow, as observed in the experiment, of $M \sim 1.1$ will become sub-sonic at a point $y_{sonic} = \frac{45}{1024}(F/\#)\lambda/(\frac{\langle U\rangle}{T_e})^2 \left(M(2M^2-5)\sqrt{M^2-1}+3ln\left[\sqrt{M^2-1}+M\right]\right)$ after entering the laser spot. Using the experimental values $I_{\rm UV}^{\rm heater} = 1.4\times10^{15}$ W/cm^2, $T_e = 1.2$ keV, and $F/\# = 1.8$ the normalized ponderomotive potential was $\langle U\rangle/T_e = 0.013$. An estimate was made for the temperature within the crossing beam region when the shock is generated. This temperature will be between the value measured upstream, 0.9 keV, and the 1.5 keV of the hot plasma observed exiting the crossing beam region at 8 ns. Here the $F/\#$ has been reduced from the individual beam value of 6.7 to 1.8 in order to account the reduction in speckle size due to 18 overlapping beams. When using overlapped speckled beams the intensity profiles must be summed, this produces smaller speckles with steeper gradients [18]. This produces a $y_{sonic} = 5$ μm, which is much smaller then the spot size of 300 μm.

Figures 5(a) and 5(b) show density and flow velocity cross-sections along the flow direction, away from the target, from the CLAWPACK simulation. Here $y = 0\mu$m corresponds to the foil facing edge of the heating beams, and $t = 0$ns in the simulation corresponds to 7.0 ns in the

experiment where the Mach number of the incoming flow stabilizes. The region within the beam has been shaded and shows rapid oscillations of the flow and density associated with the effects of individual speckles. The obtained $y_{sonic} \approx 3.5\mu m$, denoted by the green dashed line, in these figures is within the confidence interval of the theoretical prediction $\approx 5\mu m$, due to the statistical variation of the configuration of the speckles which can slightly alter the y_{sonic}. The time required for the shock to coalesce from the action of many speckle and to emerge from the laser spot, referred to as the shock breakout time, is observed in simulations at $t \approx 340$ps [Fig. 5(a) and Fig. 5(b)]. This can be observed in the transition from the black to blue to orange curves showing the growth of a feature at $\approx 3.5\mu m$ which is distinct from the noisy pattern which is the direct response of the plasma to the individual speckles. This feature then breaks out and is freely propagating in the red curve. The free-propagating shock, is moving super-sonically against the incoming super-sonic flow, resulting in a front that moves at a net speed of $-0.03c_s$, consistent with the Rankine-Hugoniot relations [8]. It takes approximately 700ps for the shock to travel $5\mu m$ from the beam boundary. This time is again shorter then the pulse duration of the heating beams which provide the ponderomotive force. Shock speed is also consistent with the experimentally observed delay between the flow reaching $M = 1.1$ and becoming subsonic when the shock reaches the Thomson scattering volume in Figure 3(b). The influence of the lasers can also be seen propagating downstream and exiting the beam profile by 340 ps, as shown by the orange curve.

Further simulations were performed using the particle-in-cell code VPIC [19–21] with a full Maxwell field solver that self-consistently includes the ponderomotive force on the slow (ion) time scale. These kinetic simulations use a 2D domain of 91 × 186 µm. These simulations are rotated 90 °relative to the CLAWPACK simulations capturing the flow and laser propagation directions. A speckled laser beam of average intensity 1.4×10^{15} W/cm^2 with vacuum wavelength $\lambda_0 = 351$ nm is launched in the direction orthogonal to the flow with width extending from -60 to -10 µm as shown in Fig. 6. The plasma at $n_e = 0.01n_c$ is comprised of electrons and Al^{+11} ions with reduced mass ratio $m_i/m_e = 2511$ and a Mach 1.1 supersonic flow. Absorbing boundaries for the electromagnetic fields and particles are used, and electron and ion inflows at the supersonic value are prescribed at the boundaries. 512 electron macroparticles/cell were used, and the ion macroparticles were represented as having identical statistical weights as the electrons (thus preserving exact momentum and energy conservation in the binary collision model[22]). The initial temperatures are Te = 800 eV and Ti = 80eV; however, the electrons are heated by the laser to 1.2 keV prior to the shock formation. Similarly to the theoretical model, the beam in simulation is treated as $F/\# = 1.8$

Figures 6(a) and 6(b) show density and flow velocity cross-sections along the flow direction, away from the target, from the VPIC simulation. The VPIC simulations were similarly able to qualitatively capture most of the features observed in the experiment (Figs. 3, 4). From the initial 5ps curve (black) to the 50ps curve (green) the density and flow perturbation grow, then break out of the laser spot around 105ps (red). Again, a density deficit can be observed forming downstream of the crossing beams, as was observed in Figure 4(a). The magnitude of this shock of 1.5× is still smaller than observed in the experiment but larger than what was observed in CLAWPACK simulations, figure 5. The VPIC simulations show better agreement with the measured shock magnitude, though the reduced mass ratio and smaller beam width (necessary to make the simulations tractable) may prevent reproducing the data quantitatively. This qualitative comparison with the data supports the premise that the inclusion of the ponderomotive force is sufficient to generate the shock.

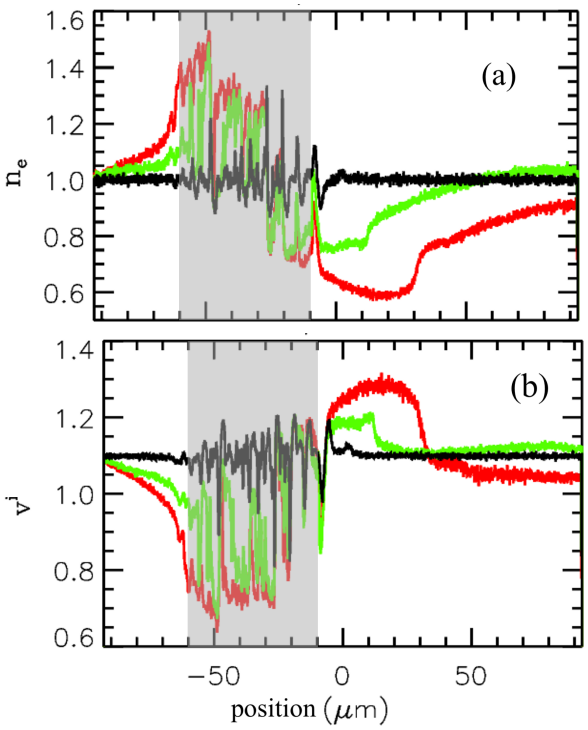

FIG. 6. VPIC simulations including the ponderomotive force. (a) electron density normalized to the background density of 1.0×10^{20} cm^{-3} and (b) flow velocity normalized to the sound speed as a function of position along the flow direction. Three temporal slices, at 5ps (black), 50ps (green), and 105ps (red) are shown. The shaded regions are within the beam spot.

High intensity laser beams in a flowing plasma have been shown to produce a shock due to the ponderomotive force. A shock front, characterized by a density spike and a transition from super-sonic to sub-sonic flow, was observed in Thomson scattering data, and was identified as traveling upstream since it only appears in the presence of the 18 high-intensity crossing beams. Comparisons with hydrodynamic simulations from GORGON shows

the shock does not originate from the target itself or the inverse bremsstrahlung heating of the crossing beams, as GORGON shows no shocks in the system. Simulations with CLAWPACK and VPIC show that the ponderomotive force alone is able to reproduce a shock feature and VPIC suggests the shock strength is dependent on thermal enhancement of the ponderomotive action. Combining the data and simulations the shock is identified to originate from the ponderomotive action of the 18 crossing beams on the super-sonically flowing plasma. Situations of high intensity lasers in a flowing plasma are common to laser based inertial confinement fusion schemes and most integrated modeling does not include ponderomotive effects. The presence of this effect may impact hydrodynamics, beam propagation, and lead to beam deflection that is not captured in current models.

The data that supports the findings of this study are available within the article, further data is available from the corresponding author upon request.

This work was performed under the auspices of the U.S. Department of Energy by Lawrence Livermore National Laboratory (LLNL) under Contract No. DE-AC52-07NA27344. This work was supported by LLNL's WPD & ICF Program's Academic Collaboration Teams's University Program (ACT-UP) under Subcontract No. B645970. This material is based upon work supported by the Department of Energy [National Nuclear Security Administration] University of Rochester "National Inertial Confinement Fusion Program" under Award Number(s) DE-NA0004144. LANL work was performed under the auspices of the U.S. Dept. of Energy by the Triad National Security, LLC Los Alamos National Laboratory and was supported by the LANL Office of Experimental Sciences Inertial Confinement Fusion program. Computing resources for VPIC simulations were provided by ATCC and LANL Institutional Computing programs.

AM was the principal investigator for the experimental campaign. CB worked on the experimental design and data analysis. CW and SH provided simulations, with WF performing supporting simulations. LY and BA provided the VPIC simulations. JL, HR, SH, and WR helped with conceptualization and theory. And GS helped with data analysis and provided experimental time.

[1] D. H. Edgell, J. Katz, R. Raimondi, D. Turnbull, and D. H. Froula, Scattered-light uniformity imager for diagnosing laser absorption asymmetries on omega, Review of Scientific Instruments **93**, 10.1063/5.0101798 (2022).

[2] W. A. Farmer, C. Bruulsema, G. F. Swadling, M. W. Sherlock, M. D. Rosen, W. Rozmus, D. H. Edgell, J. Katz, B. B. Pollock, and J. S. Ross, Validation of heat transport modeling using directly driven beryllium spheres, Physics of Plasmas **27**, 082701 (2020).

[3] A. B. Zylstra, O. A. Hurricane, D. A. Callahan, A. L. Kritcher, J. E. Ralph, H. F. Robey, J. S. Ross, C. V. Young, K. L. Baker, D. T. Casey, T. Döppner, L. Divol, M. Hohenberger, S. L. Pape, A. Pak, P. K. Patel, R. Tommasini, S. J. Ali, P. A. Amendt, L. J. Atherton, B. Bachmann, D. Bailey, L. R. Benedetti, L. B. Hopkins, R. Betti, S. D. Bhandarkar, J. Biener, R. M. Bionta, N. W. Birge, E. J. Bond, D. K. Bradley, T. Braun, T. M. Briggs, M. W. Bruhn, P. M. Celliers, B. Chang, T. Chapman, H. Chen, C. Choate, A. R. Christopherson, D. S. Clark, J. W. Crippen, E. L. Dewald, T. R. Dittrich, M. J. Edwards, W. A. Farmer, J. E. Field, D. Fittinghoff, J. Frenje, J. Gaffney, M. G. Johnson, S. H. Glenzer, G. P. Grim, S. Haan, K. D. Hahn, G. N. Hall, B. A. Hammel, J. Harte, E. Hartouni, J. E. Heebner, V. J. Hernandez, H. Herrmann, M. C. Herrmann, D. E. Hinkel, D. D. Ho, J. P. Holder, W. W. Hsing, H. Huang, K. D. Humbird, N. Izumi, L. C. Jarrott, J. Jeet, O. Jones, G. D. Kerbel, S. M. Kerr, S. F. Khan, J. Kilkenny, Y. Kim, H. G. Kleinrath, V. G. Kleinrath, C. Kong, J. M. Koning, J. J. Kroll, M. K. Kruse, B. Kustowski, O. L. Landen, S. Langer, D. Larson, N. C. Lemos, J. D. Lindl, T. Ma, M. J. MacDonald, B. J. MacGowan, A. J. Mackinnon, S. A. MacLaren, A. G. MacPhee, M. M. Marinak, D. A. Mariscal, E. V. Marley, L. Masse, K. Meaney, N. B. Meezan, P. A. Michel, M. Millot, J. L. Milovich, J. D. Moody, A. S. Moore, J. W. Morton, T. Murphy, K. Newman, J. M. D. Nicola, A. Nikroo, R. Nora, M. V. Patel, L. J. Pelz, J. L. Peterson, Y. Ping, B. B. Pollock, M. Ratledge, N. G. Rice, H. Rinderknecht, M. Rosen, M. S. Rubery, J. D. Salmonson, J. Sater, S. Schiaffino, D. J. Schlossberg, M. B. Schneider, C. R. Schroeder, H. A. Scott, S. M. Sepke, K. Sequoia, M. W. Sherlock, S. Shin, V. A. Smalyuk, B. K. Spears, P. T. Springer, M. Stadermann, S. Stoupin, D. J. Strozzi, L. J. Suter, C. A. Thomas, R. P. Town, E. R. Tubman, P. L. Volegov, C. R. Weber, K. Widmann, C. Wild, C. H. Wilde, B. M. V. Wonterghem, D. T. Woods, B. N. Woodworth, M. Yamaguchi, S. T. Yang, and G. B. Zimmerman, Burning plasma achieved in inertial fusion, Nature **601**, 542 (2022).

[4] H. A. Rose, Laser beam deflection by flow and nonlinear self-focusing, Physics of Plasmas **3**, 1709 (1996).

[5] S. Ghosal and H. A. Rose, Two-dimensional plasma flow past a laser beam, Physics of Plasmas **4**, 2376 (1997).

[6] S. Hüller, G. Raj, W. Rozmus, and D. Pesme, Crossed beam energy transfer in the presence of laser speckle ponderomotive self-focusing and nonlinear sound waves, Phys. Plasmas **27**, 022703 (2020).

[7] W. A. Farmer, C. Ruyer, J. A. Harte, D. E. Hinkel, D. S. Bailey, E. Kur, O. L. Landen, N. Lemos, P. A. Michel, J. D. Moody, D. J. Strozzi, C. R. Weber, and G. B. Zimmerman, Impact of flow-induced beam deflection on beam propagation in ignition scale hohlraums, Physics of Plasmas **31**, 022705 (2024).

[8] J. D. Ludwig, S. Hüller, H. A. Rose, C. Bruulsema, W. Farmer, P. Michel, A. L. Milder, G. F. Swadling, and W. Rozmus, Shock formation in flowing plasmas by temporally and spatially smoothed laser beams, Phys. Plasmas **31**, 032103 (2024).

[9] S. Hüller, J. D. Ludwig, H. A. Rose, C. Bruulsema, W. Farmer, P. Michel, A. L. Milder, G. F. Swadling, and W. Rozmus, Modeling and simulations of hydrodynamic shocks in a plasma flowing across randomized icf scale laser beams, Comptes Rendus. Physique **25**, 353-365 (2024), https://doi.org/10.5802/crphys.200.

[10] T. R. Boehly, R. S. Craxton, T. H. Hinterman, J. H. Kelly, T. J. Kessler, S. A. Kumpan, S. A. Letzring, R. L. McCrory, S. F. B. Morse, W. Seka, S. Skupsky, J. M. Soures, and C. P. Verdon, The upgrade to the omega laser system, Review of Scientific Instruments **66**, 508 (1995).

[11] J. P. Chittenden, S. V. Lebedev, C. A. Jennings, S. N. Bland, and A. Ciardi, X-ray generation mechanisms in three-dimensional simulations of wire array z-pinches (2004).

[12] D. H. Froula, S. H. Glenzer, J. N. C. Luhmann, and J. Sheffield, *Plasma Scattering of Electromagnetic Radiation: Theory and Measurement Techniques*, 2nd ed. (Academic Press, 2011).

[13] C. A. Walsh, J. P. Chittenden, K. McGlinchey, N. P. Niasse, and B. D. Appelbe, Self-generated magnetic fields in the stagnation phase of indirect-drive implosions on the national ignition facility, Physical Review Letters **118**, 10.1103/PhysRevLett.118.155001 (2017).

[14] C. A. Walsh, J. P. Chittenden, D. W. Hill, and C. Ridgers, Extended-magnetohydrodynamics in underdense plasmas, Physics of Plasmas **27**, 10.1063/1.5124144 (2020).

[15] P. T. Campbell, C. A. Walsh, B. K. Russell, J. P. Chittenden, A. Crilly, G. Fiksel, P. M. Nilson, A. G. Thomas, K. Krushelnick, and L. Willingale, Magnetic signatures of radiation-driven double ablation fronts, Physical Review Letters **125**, 10.1103/PhysRevLett.125.145001 (2020).

[16] P. T. Campbell, C. A. Walsh, B. K. Russell, J. P. Chittenden, A. Crilly, G. Fiksel, L. Gao, I. V. Igumenshchev, P. M. Nilson, A. G. Thomas, K. Krushelnick, and L. Willingale, Measuring magnetic flux suppression in high-power laser-plasma interactions, Physics of Plasmas **29**, 10.1063/5.0062717 (2022).

[17] R. J. L. Vecque, Wave propagation algorithms for multidimensional hyperbolic systems, J. Comp. Phys. **131**, 327 (1997).

[18] H. A. Rose, D. F. DuBois, Collective filamentation in induced spatial incoherence and multiple laser beam configurations, Phys. Fluids B **4**, 252 (1992).

[19] K. J. Bowers, B. J. Albright, L. Yin, B. Bergen, T. J. T. Kwan, Phys. Plasmas **15**, 055703 (2008).

[20] K. J. Bowers, B. J. Albright, B. Bergen, L. Yin, K. J. Barker and D. J. Kerbyson, Proc. 2008 ACM/IEEE Conf. Supercomputing 63, 1 (2008). http://dl.acm.org/citation.cfm?id=1413435

[21] K. J. Bowers, B. J. Albright, L. Yin, W. Daughton, V. Roytershteyn, B. Bergen and T. J. T. Kwan, Journal of Physics: Conference Series 180, 012055 (2009).

[22] T. Takizuka and H. Abe, J. Computat. Phys. **25**, 205 (1977).